Computers in Biology and Medicine 39 (2009) 1137–1144

Contents lists available at ScienceDirect

Computers in Biology and Medicine

journal homepage: www.elsevier.com/locate/cbm

Pleural nodule identification in low-dose and thin-slice lung computed tomography

A. Retico [a,*], M.E. Fantacci [a,b], I. Gori [a,c], P. Kasae [d], B. Golosio [d,e], A. Piccioli [d,e], P. Cerello [f], G. De Nunzio [g,h], S. Tangaro [i]

[a] Istituto Nazionale di Fisica Nucleare, Sezione di Pisa, Italy
[b] Dipartimento di Fisica, Università di Pisa, Italy
[c] Bracco Imaging S.p.A., Milano, Italy
[d] Istituto Nazionale di Fisica Nucleare, Sezione di Cagliari, Italy
[e] Dipartimento di Matematica e Fisica, Università di Sassari, Italy
[f] Istituto Nazionale di Fisica Nucleare, Sezione di Torino, Italy
[g] Dipartimento di Scienza dei Materiali, Università del Salento, Italy
[h] Istituto Nazionale di Fisica Nucleare, Sezione di Lecce, Italy
[i] Istituto Nazionale di Fisica Nucleare, Sezione di Bari, Italy

ARTICLE INFO

Article history:
Received 27 October 2008
Accepted 9 October 2009

Keywords:
Computer-aided detection (CAD)
Low-dose computed tomography (LDCT)
Thin-slice CT
Lung nodule
Directional-gradient concentration
Morphological operators
Neural networks

ABSTRACT

A completely automated system for the identification of pleural nodules in low-dose and thin-slice computed tomography (CT) of the lung has been developed. The *directional-gradient concentration* method has been applied to the pleura surface and combined with a morphological *opening*-based procedure to generate a list of nodule candidates. Each nodule candidate is characterized by 12 morphological and textural features, which are analyzed by a rule-based filter and a neural classifier. This detection system has been developed and validated on a dataset of 42 annotated CT scans. The *k*-fold cross validation has been used to evaluate the neural classifier performance. The system performance variability due to different *ground truth agreement levels* is discussed. In particular, the poor 44% sensitivity obtained on the *ground truth with agreement level* 1 (nodules annotated by only one radiologist) with six FP per scan grows up to the 72% if the underlying *ground truth* is changed to the *agreement level* 2 (nodules annotated by two radiologists).

1. Introduction

Lung cancer is one of the most lethal kinds of cancer worldwide. The overall 5-year survival rate is only 10–15% [1,2] and no significant improvement has occurred in the last 20 years [3]. Non-calcified small pulmonary nodules are considered as the primary signs of early-stage lung cancers. Computed tomography (CT) has been shown to be the most sensitive imaging modality for detecting small pulmonary nodules, particularly since the introduction of the multi-detector-row and helical CT technologies [4]. The efficacy of screening trial protocols based on low-dose CT with thin reconstructed slice thickness in reducing the lung cancer mortality rate are currently under investigation in many developed countries [5–8]. Depending on the screening trial protocol, the radiologists may have to identify even very small nodules, carrying out an extremely difficult and time-consuming task. Nodules are rather spherical or hemispherical objects that can be characterized by low CT values and/or low contrast. They may have CT values in the same range of those of blood vessels and airway walls and may be strongly connected to them or to the pleura surface. The nodule identification in screening CT is particularly difficult as low-dose CT images show a noisier appearance with respect to the standard-dose ones and an amount of image data as large as about 300 2D slices per scan may be generated in case thin reconstructed slice thickness is used.

To support radiologists in the challenging task of interpreting screening lung CT scans, researchers explore computer-aided detection (CAD) methods devoted to the automated identification of possibly pathological objects in the images. In this framework, an automated procedure for the detection of lung nodules embedded in the lung parenchyma has already been developed by our group, and described in [9,10]. That system is devoted to the identification of almost spherical shaped nodules, which can be either isolated, i.e. not connected to the surrounding anatomical structures, or attached to blood vessels and fissures, or connected to the pleura surface by a tail. The main steps of that analysis are a filter based on the eigenvalues of the Hessian matrix

* Corresponding author.
E-mail address: alessandra.retico@pi.infn.it (A. Retico).

0010-4825/$ - see front matter © 2009 Elsevier Ltd. All rights reserved.
doi:10.1016/j.compbiomed.2009.10.005

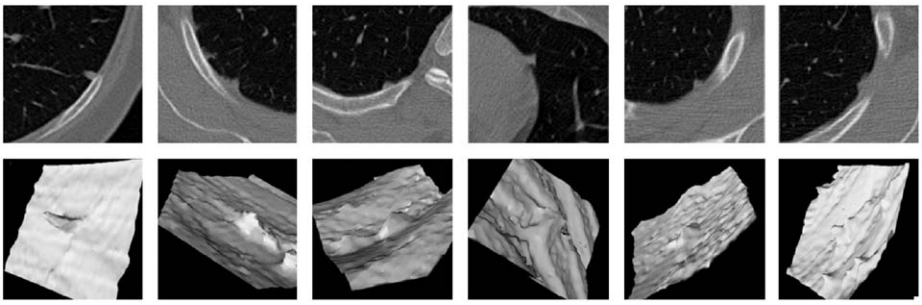

Fig. 1. Examples of pleural nodules: nodule appearance in 2D CT slices (top) and the corresponding shaded surface display representations (bottom).

to enhance spherical objects [11], and an original voxel-based neural approach (VBNA) to reduce false-positive detections. The system we present in this paper is instead devoted to the automated identification of pleural nodules only, i.e. nodules deeply connected to the pleura surface. They are characterized by a rather hemispherical shape, as they originate in the pleura surface and grow toward the lung parenchyma. Examples of the pleural nodule appearance in 2D CT slices and the corresponding shaded surface display representations are shown in Fig. 1. The approach we followed to identify this type of nodules is completely different from that we used for nodules embedded in the lung parenchyma. In this case, the analysis is focused on the curvature of pleura surface, and a regional feature-based approach instead of a voxel-based one is implemented to reduce the amount of false-positive detections. We designed a dedicated system to identify pleural nodules as they are different in morphology with respect to nodules embedded in the lung parenchyma. Dealing with each nodule category with different dedicated CAD systems and combining their results can lead to a possible improvement in lung nodule automated detection.

This paper is structured as follows: the dataset we used in this analysis is described in Section 2, the CAD algorithm is presented in Section 3, and the final system results are reported in Section 3.3.

2. The dataset of lung CT scans

The dataset of lung CTs used to develop, test and validate the CAD system was acquired by means of a helical 4-slice CT scanner (Siemens Volume Zoom) according to a low-dose protocol (tube voltage: 140 kV, tube current: 20 mA, mean equivalent dose 0.6 mSv, scanning time: 6–8 s), with 1.25 mm slice collimation. Each scan is stored in DICOM format [12]. Slices were reconstructed at 1 mm thickness, using a medium sharp reconstruction kernel (Siemens B50f). The number of slices per scan is 312 ± 18, each slice being a 512×512 pixel matrix, with pixel sizes ranging from 0.53 to 0.74 mm and 12 bit gray levels in Hounsfield units. The dataset used in this analysis consists of 42 CT scans.

The dataset annotation was provided by two experienced radiologists participating to our research project. The software we developed for annotating the CT scans allows the radiologists to draw a circle enclosing a selected object on a CT slice; then, a 3D viewer is popped-up on demand to allow the size and location adjusting of the annotating sphere according to the nodule appearance in 3D. In the case of pleural nodules, the annotated diameters very often provide an overestimate of the nodule size. We considered for this study only the pleural nodules characterized by an annotated diameter greater than 5 mm.

To build a reference standard with nodules annotated either by only one or by both radiologists, we followed the method introduced in Opfer et al. [13]. We call *ground truth with agreement level j* the list of all nodules which are marked by at least j of the radiologists who performed the CT annotation; $j = 1, 2$ in our study. The dataset of 42 CT scans considered in this analysis contains 102 solid pleural nodules according to the *ground truth with agreement level* 1 and 25 solid pleural nodules according to the *agreement level* 2. It can be observed that there is a substantial interreader variability, reflecting the difference in opinion even among radiologists with a similar degree of experience. The issue of interreader variability is widely recognized in both the detection and boundary delineation of lung nodules on CT [13–15]. The degree of agreement we found between the annotations performed by the two readers involved in our study is consistent with the percentages reported by other studies [13–15].

The average diameter of the annotated nodules is 7.6 mm with 4.0 mm standard deviation at the *agreement level* 1, whereas it is 5.6 mm with 2.4 mm standard deviation at the *agreement level* 2. We noticed that some very large abnormalities marked at the *agreement level* 1 were not confirmed as nodules at the *agreement level* 2.

3. The CAD system

The CAD strategy we implemented to identify the pleural nodules is shown in the block diagram reported in Fig. 2. It is based on the following steps:

- A list of regions of interest (ROIs) is obtained by applying a two-step procedure: first, the pleura is identified by an iso-surface triangulation technique; then, the ROIs are provided by the *directional-gradient concentration* method combined to a morphological *opening* operation.
- The false-positive (FP) findings populating the ROI list are ruled out by the following method: 12 geometrical and textural features are computed on the nodule candidate segmented out of each ROI; finally, a rule-based filter followed by a neural classification generate the list of CAD findings.

All steps of the analysis are detailed below.

3.1. Identification of nodule candidates: the ROI hunter procedure

A crucial task in the development of a CAD scheme for nodule detection is the initial selection of nodule candidates, which was carried out by means of a 3-step ROI hunter algorithm. For each CT scan it provides a list of the locations of the nodule candidates, expressed in terms of the x, y and z coordinates of their centers.

3.1.1. Identification of the pleura surface

The pleura has been identified as the separating surface between the lung parenchyma and the surrounding soft tissues.

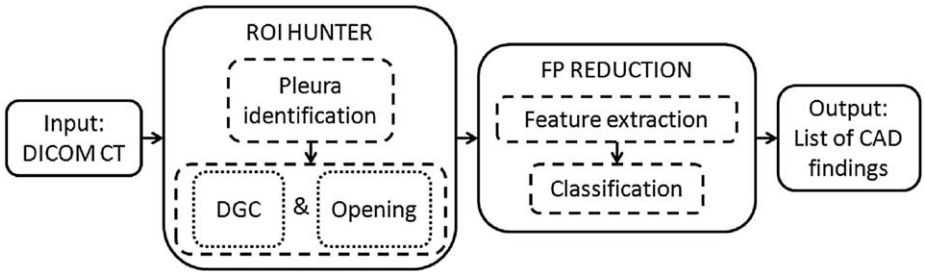

Fig. 2. Block diagram of the main steps of our CAD.

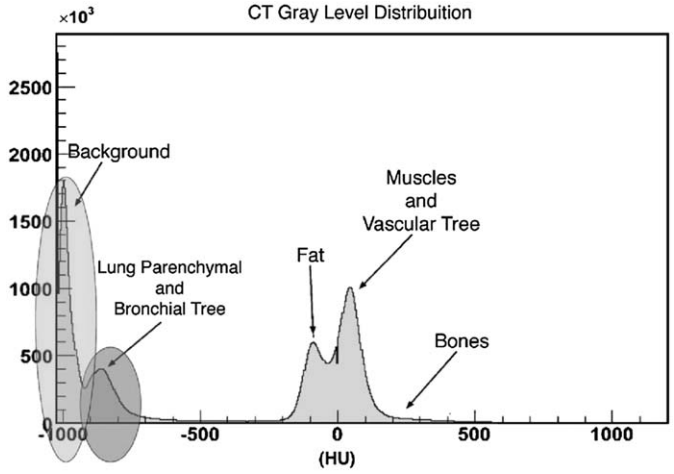

Fig. 3. Gray-level distribution of the voxel intensities in HU obtained for one CT scan of our dataset. Similar distributions can be obtained from the other CTs.

It has been determined according to an iso-surface triangulation technique.

Given a value μ_I (*iso-value*), the iso-surface corresponding to μ_I is defined as the set of points satisfying the equation $\mu(x,y,z)=\mu_I$. Such equation defines a surface that separates volumes having density greater than μ_I from volumes having density lower than μ_I. As shown in Fig. 3 reporting the intensity distribution of $\mu(x,y,z)$ for one CT scan of our dataset, the lung parenchyma has a very low mean density (lower than −800 HU), while the soft tissues have a mean density around zero HU. To separate the lung parenchyma from the soft tissues, the value $\mu_I=-500$ HU can be used, as it corresponds approximately to the average between the mean densities of these tissues.

A discrete representation of an iso-surface can be obtained by approximating it by a set of small triangular facets. Such procedure is called iso-surface triangulation. To represent the iso-surface obtained for $\mu_I=-500$ HU, we used the popular marching-cube algorithm [16,17]. The output of the triangulation algorithm is a collection of triangular facets, which are clusterized into connected components by forcing two triangles into the same component when they have at least one edge in common. The volume enclosed by each of these connected surfaces is evaluated. By convention, the sign is taken as positive if the intensity values inside the surface are above the threshold (and thus the region outside has values below the threshold), negative otherwise. For example, the surface corresponding to the epidermis has a positive sign, since it is surrounded by air, which is surely below the threshold. The surface separating the lung parenchyma from the surrounding soft tissues is identified as the connected surface having the negative volume of largest magnitude. A mask for the lung parenchyma is obtained by flood-filling the volume inside such surface. At this stage, vessels and airway walls are not included in the mask. To include them, a procedure based on morphological operators was developed. In particular, the dilation operator with a spherical kernel of 10 voxels of diameter is applied to fill in the vessels and the airway walls, then, the erosion operator with spherical kernel of 20 voxels of diameter strongly erodes the mask border. Finally, the logical OR operation between the so-obtained mask and the original lung mask provides the final mask where the vessels and the airway walls are filled in, while maintaining the original shape of the lung mask border, i.e. the shape of the pleural nodule is not modified by this procedure.

3.1.2. Directional-gradient concentration (DGC)

To identify the ROIs where pleural nodules can be located, we implemented the *directional-gradient concentration* (DGC) method [18,19], applied to the pleura surface. As pleural nodules are usually characterized by a convex surface, the inward-pointing fixed-length surface normal vectors $N(x,y,z)$ crossing the nodule surface tend to intersect within the nodule tissue. A 3D array, denoted as $A(x,y,z)$, counts the number of surface normals passing through each voxel, i.e. each voxel accumulates a score proportional to the number of surface normals that pass through it (see the 2D sketch in Fig. 4). The larger the number of the line segments passing through a voxel, the higher the score the voxel has in the A matrix. The local maxima in the A matrix represent the convex regions characterizing pleural nodules or irregularities in the pleura surface. The DGC procedure has only one free parameter, which is the length of the surface normal vector. We fixed this parameter to $l=9$ mm, as this value enables the detection of nodules with effective diameters in the range of those annotated in our dataset. We also verified that higher values of l lead to an increase of noisy entries into the ROI list, whereas lower values of l do not allow the normal vector overlap in correspondence to large nodules.

We found out that many local maxima of the A matrix are irregularities located in correspondence to the mediastinal pleura. As shown in Fig. 5, the surface representing the mediastinal pleura in our CT scans is characterized by many folds and ridges, which are artifacts probably generated by the heart beating. The 3D DGC procedure is sensitive to these ridge-shaped artifacts, as they provide counts in the A matrix in the same range of the nodules. However, as they have the principal direction corresponding to the maximum curvature along the z axis, these artifacts will not affect a 2D slice-wise analysis. Thus we decided to combine the DGC method with a specific 2D procedure, as described in the following section.

3.1.3. Matching with the morphological opening-based procedure

A morphological *opening* operation has been implemented slice wise following the schema reported in Fig. 6 and described below:

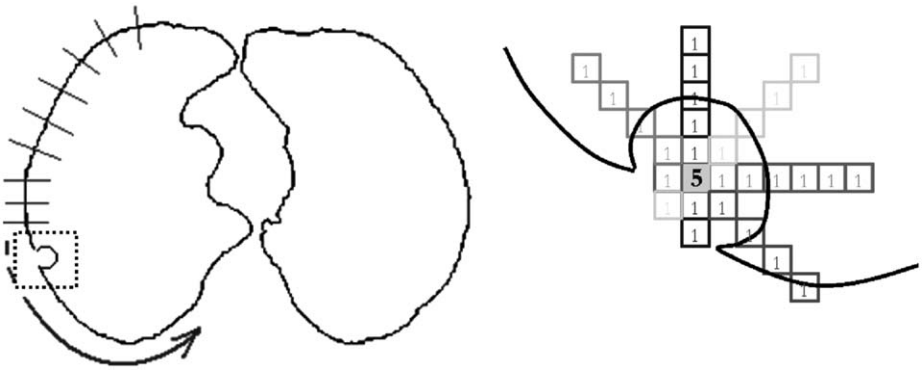

Fig. 4. Sketch of the DGC procedure: each voxel of the $A(x,y,z)$ matrix accumulates a score proportional to the number of surface normals that pass through it. For example, if five line segments pass through the central voxel of a pleural nodule, the score 5 will be assigned to that voxel.

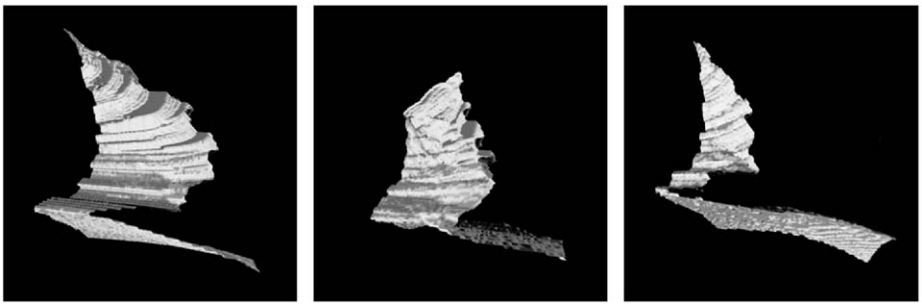

Fig. 5. Appearance of the mediastinal pleura in a CT scan: the flatness of the diaphragmatic pleura can be compared with the knurled surface representing the mediastinal pleura.

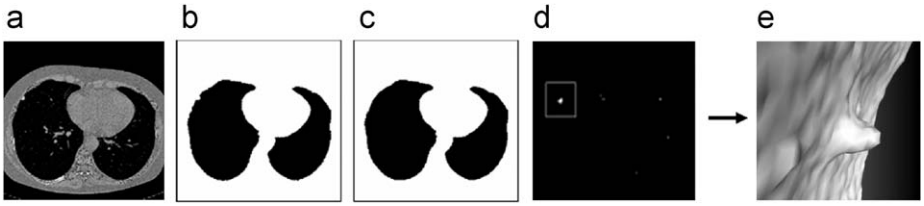

Fig. 6. Morphological *opening*-based procedure applied to a CT slice: (a) a slice of the original CT scan; (b) binary conversion of the slice once the pleura has been identified; (c) *opened* image; (d) the image in (c) is subtracted from the image in (b) and (e) shaded surface display representation of one nodule candidate.

- the image obtained after the identification of the pleura surface is converted to a binary mask setting to 1 the region outside the pleura and to 0 the region inside;
- the morphological *opening* operator is applied slice wise to this mask by using a circular disk as structuring element;
- the *opened* image is then subtracted from the binary mask slice by slice;
- the sequence of 2D images obtained is recombined in a 3D array, denoted as $B(x,y,z)$.

The only parameter introduced in this procedure is the size of the circular disk used as structuring element in the *opening* operation. We fixed the disk diameter to $d_{\text{disk}} = 11$ mm, as we have verified that using higher values of d_{disk} would include in $B(x,y,z)$ unwanted portions of tissues, such as the section of the vascular tree near the lung hilum.

The logical AND operation is then implemented between the A and the B matrices. A peak-detector algorithm is applied to A AND B to detect the local maxima and create the list of ROIs, identified by the coordinates of their centers and sorted according to the value of the score reported in A.

To assess the efficiency of our ROI hunter, we define as true positives (TPs) the nodule candidates that meet the radiologists' diagnosis according to the following condition: the Euclidean distance between the coordinates (x,y,z) of the nodule candidate center and the center $(x_{\text{rad}}, y_{\text{rad}}, z_{\text{rad}})$ of the radiologists' drawn circle has to be smaller than the radius R_{rad} reported in the radiologists' annotation. All the other candidates are considered as false positives (FPs).

According to the above-mentioned definitions, the efficiency of the ROI hunter is $\varepsilon = 94.1\%$, corresponding to 96 correctly identified pleural nodules out of the 102 annotated in our dataset according to the *ground truth with agreement level* 1. By contrast, $\varepsilon = 1$ according to the *ground truth with agreement level* 2. At this stage the average number of FPs per CT is 546.

3.2. False-positive finding reduction

The procedure we implemented to reduce the FP entries in the ROI list consists in the classification of 12 morphological and textural features extracted from each nodule candidate.

3.2.1. Feature extraction

To obtain a segmentation mask of each nodule candidate in order to extract the features, we exploited the output of the

previously described *opening*-based procedure. We selected the 3D objects in the *B* matrix which are connected to the coordinates of each entry of the ROI list.

Twelve common features based on the geometrical and the textural characteristics of the so segmented nodule candidates are computed:

1–4 the *average*, the *standard deviation*, the *skewness* and the *kurtosis* of the density distribution of the nodule candidate, expressed in HU;
5–6 the *minimum* and the *maximum value* of the density distribution of the nodule candidate, expressed in HU;
7 the *volume* of the nodule candidate, simply estimated by counting the number of voxels of the segmented mask, and converting it to a physical volume (mm^3) by multiplying it by the voxel volume;
8 the *volume* of the 3D nodule candidate *convex hull*, estimated according to the *Qhull* software [20,21] and converted to a physical volume (mm^3);
9 the *volume* of the nodule candidate *minimum enclosing ball*, evaluated according to the technique and the code developed by P. Kumar, J.S.B. Mitchell and E.A. Yildirim [22];
10–12 the *three eigenvalues* of the *covariance matrix* of the nodule candidate coordinates, which provide a rotational invariant measure of the object extension along three orthogonal axes.

3.2.2. Feature classification

The procedure we implemented to reduce the FP entries from the list of nodule candidates consists in a rule-based filter followed by a neural classification of the feature vectors.

As a large number of FP findings are characterized by either a very small or a very large size, a simple rule-based filter can easily eliminate them from the list of nodule candidates. Performing the initial FP removal by means of a rule-based scheme is an approach implemented by several other lung CAD developers [23–25]. A double-threshold cut on the volume (V) of the segmented nodule candidates and on the volume of their minimum enclosing ball (V_{meb}) has been implemented in our work. The lower and upper limits on V and V_{meb} have been *a priori* determined according to the criterion that CAD has to be sensitive to pleural nodules in the size range limited by the values of V and V_{meb} of the smallest and of the largest nodule of the available dataset. Whenever a nodule candidate is characterized by either V or V_{meb} out of the allowed range it is considered as an FP and eliminated from further processing. This rule-based filter is able to eliminate the 26.8% of the FPs from the list of nodule candidates. The remaining 400 FPs/scan on average are further analyzed by a neural classifier.

As the amount of the ROIs containing FPs (16 782) is about two orders of magnitude larger than that of the ROIs containing nodules (96 according the *ground truth with agreement level* 1), only a small percentage of patterns derived from FP regions has to be considered to create a balanced dataset to train and validate the neural networks. To this aim we used a self-organizing map (SOM) [26]. Through an unsupervised learning procedure based on the *winner-takes-all* rule, this kind of network clusterizes the input data into the cells of the *Kohonen layer*, according to a similarity criterion. We provided the entire FP dataset to an SOM, thus obtaining the clusterization of the FP feature vectors into 3×3 cells. By extracting a small percentage (1.5%) of the entries from each cell, we collected a sample of the FPs, which is representative of the entire FP dataset. This dataset of 246 FP patterns, in addition to the 96 nodule patterns, constitutes the dataset we used to train and validate the neural classification procedure.

The neural networks we implemented are standard supervised three-layered feed-forward neural networks (12 input, 14 hidden, 1 output units), trained with the back-propagation learning algorithm. The k-fold cross validation [27] with $k = 10$ has been implemented to evaluate the neural classifier performance. This method is used to determine how accurately a learning algorithm is able to predict the data it was not trained on. When using the k-fold method, the dataset is randomly partitioned into k groups. The neural classifier is then trained k times, using all data except those in the k th group, and then run on the k th set. The mean performance obtained over all k sets is evaluated in terms of the receiver operating characteristic (ROC) analysis [28], which provides more information than just a single sensitivity and specificity pair to describe the accuracy of a diagnostic test. Moreover, as it would be helpful to assess the performance of a diagnostic test by a single number, we derived the area under the ROC curve (AUC). The meaning of the AUC has been proved to be the probability that a random pair of positive/diseased and negative/non-diseased individuals would be identified correctly by the diagnostic test [29]. We obtained an average $AUC = 0.88$ over the 10 validation sets, with a standard deviation $\sigma_{AUC} = 0.07$.

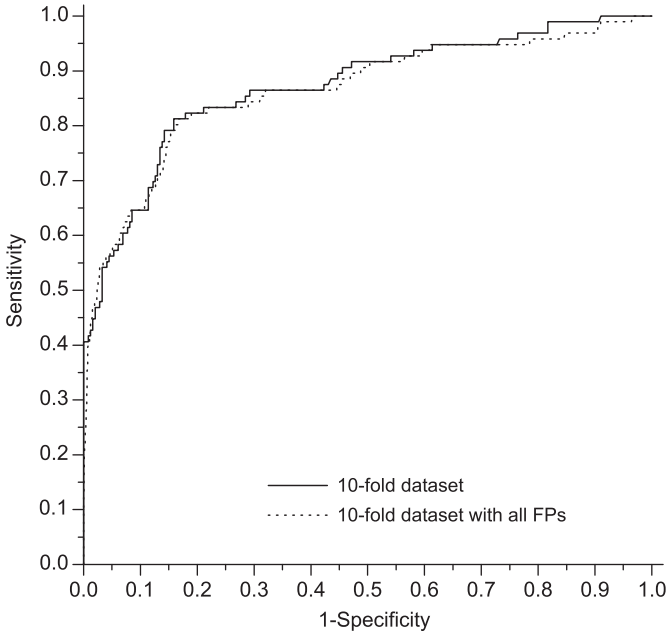

Fig. 7. The ROC curves obtained on the 10-fold dataset and on the entire dataset including all FPs generated by the ROI hunter.

We also computed the ROC curve for the complete dataset used in the 10-fold procedure, by collecting the neural output obtained on each fold. This ROC, which has $AUC = 0.872 \pm 0.024$, is reported in Fig. 7.

To classify the large set of FPs we had left apart during the sample extraction with the SOM (the 98.5% of FPs) we applied a simple meta-classification procedure. We assigned to each FP the average of the output obtained by the 10 trained neural classifiers. The ROC obtained has $AUC = 0.865 \pm 0.024$, as reported in Fig. 7. The error on the AUC is computed according to Ref. [30]. It can be noticed that the two values of AUC obtained are consistent, which confirms that the FP sample extracted with the SOM (1.5% of all FPs) is representative of the entire FP dataset, thus allowing a proper train and generalization capability of the neural classifiers.

3.3. Results

We assessed the final system performance in terms of the free-response operating characteristic (FROC) curve, both in case we consider the *ground truth with agreement level* 1 (102 nodules

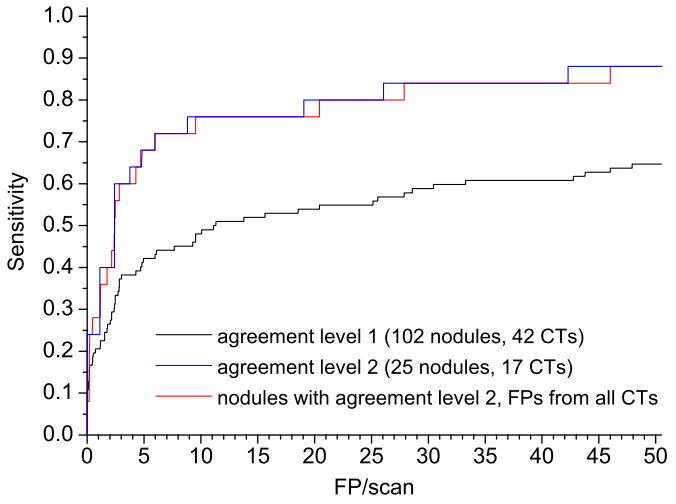

Fig. 8. FROC curves obtained on: *ground truth with agreement level* 1 (102 nodules, 42 CTs), *ground truth with agreement level* 2 (25 nodules, 17 CTs), and the dataset of 42 CTs where only nodules annotated with the *agreement level* 2 were considered.

contained in 42 CTs) and *with agreement level* 2 (25 nodules contained in 17 CTs out of the dataset of 42 CTs). The FROC curves obtained are shown in Fig. 8. In case the *ground truth with agreement level* 1 is considered, the $\varepsilon = 94.1\%$ efficiency of the ROI hunter algorithm has to be taken into account as a multiplicative factor to the values of sensitivities reported in the ROC of Fig. 7. By contrast, $\varepsilon = 1$ in case the *agreement level* 2 is considered. It can be noticed that the CAD system performance is strongly influenced by the choice of the underlying ground truth. A large discrepancy is indeed shown between the performance evaluated on the different *agreement levels* of the *ground truth*, and, as expected, the sensitivity is higher for nodules identified by both radiologists. For example, the poor 44% sensitivity obtained on the *ground truth with agreement level* 1 with six FP per scan grows up to the 72% if the underlying *ground truth* is changed to the *agreement level* 2. At that value of sensitivity, the FP rejection ability of the system reaches the 99%.

The impact on the results of including CTs with no pleural nodules could also be estimated in the case where the *ground truth with agreement level* 2 is considered. We compared the results obtained on the dataset of 17 CTs containing 25 pleural nodules (*ground truth with agreement level* 2), with the results obtained on the same dataset added by the remaining 25 CTs not containing pleural nodules (according to the *ground truth with agreement level* 2 criterion). As shown in Fig. 8, we found out that a comparable amount of FP detections is found in subjects with and without pleural nodules. This effect is probably mainly due to the fact that lung cancer screening is addressed to a high-risk population (55–69 year-old males and females, smokers or former smokers), whose pleura surface is often affected by the presence of many confounding objects, even in the absence of pleural nodules. We verified by visual inspection that the pleura surface of most subjects in our dataset, both with and without pleural nodules (*agreement level* 2), is equally affected by apical scars, pleural thickening, abnormalities next to emphysematous bullae, etc., which are the typical FP detections generated by our CAD system.

4. Conclusions and discussion

We have developed a computerized method for the automated detection of pleural nodules on low-dose and thin-slice lung CT scans. This method consists of an initial selection of a list of nodule candidates, and the classification of the 12 features computed for each segmented nodule candidate. Despite we did not carry out an extremely refined nodule segmentation procedure (e.g. that reported in Way et al. [31]), it allows to compute highly discriminant features, as confirmed by the performance achieved in classification. A dataset of 42 annotated CT scans has been used to develop, test and validate the CAD system. As this not extremely wide dataset could hardly be partitioned into equally representative subsets, the whole data took part both to the estimate of the system parameters and to the final validation. In particular, the system parameters related to the nodule size (e.g. the length of normals in the DGC method, the disk size in the opening-based procedure, the double-threshold cuts on the volumetric features) have been tuned to meet the size range of the nodules to be detected. They were *a priori* chosen according to the physical range of nodule sizes and eventually fine-tuned once verified the impact on the whole dataset. By contrast, the training of the neural classifier has been performed according to the 10-fold cross validation method, thus leaving apart a small set of validation cases in each training session. Moreover, as only the 1.5% of FP patterns extracted by the SOM have been used to train the neural network, all the remaining FP patterns actually are processed by the classifier only as validation data.

We finally showed the FROC curves we obtained on a dataset of 42 CT scans; they were evaluated at different *ground truth agreement levels*. In particular, on the *ground truth with agreement level* 1 the system does not achieve competitive values of sensitivity at an acceptable level of FP detections per scan. By contrast, the 72% sensitivity is obtained with only six FPs per scan (corresponding to 0.02 FPs per slice) on the *ground truth with agreement level* 2.

The CAD system we presented in this paper is designed as a dedicated system to pleural nodule identification. However, as much more efforts in the literature have so far gone through the simultaneous analysis of lung nodules of all categories, we are rather limited to have a vast performance comparison between our method and other CAD systems with the same purpose. Among the available CAD schemes, the one proposed by Paik et al. [18] in detecting clinically significant solid lung nodules using surface normal overlap method on datasets extracted from eight chest CTs containing 84 nodules demonstrated the 80% sensitivity to nodules with 6 mm in diameter and larger at 1.3 FPs/dataset. We could not convert this result in terms of FPs neither per scan or per slice, as the number of slices analyzed for each dataset is not reported in [18]. In a study by Lee et al. [32] on pulmonary nodules, a conventional template matching was employed to detect nodules existing on the lung wall area. A dataset of 20 clinical cases has been considered. The system sensitivity to all types of nodules is 72% at 1.1 FPs/slice. In particular, their system shows the 71% sensitivity to pleural nodules at 0.5 FPs/slice. The ability in rejecting the 88% of FPs within the detected nodule candidates is also reported. At a similar value of sensitivity (72%) our system generates only 0.02 FPs/slice, and the corresponding FP rejection ability is 99%. However, a strict quantitative comparison between our system performance and those reported in [18,32] is precluded by the difference in the CT acquisition parameters and the small number of cases collected in the dataset used in each study. A reliable comparison between our results and those reported by other research groups working on lung CAD systems could be performed only if all CAD developers run their algorithms on a common and publicly available dataset of annotated CT scan (e.g. the database provided by the Lung Imaging Database Consortium [33]). Unfortunately, a similar analysis cannot be performed at present on our CAD system as, to our knowledge, the publicly available annotated databases do not currently include the characterization of the nodule types, i.e.

it is not specified whether a nodule is either pleural or belongs to other nodule categories.

Conflict of interest statement

No conflict of interest.

Acknowledgments

This work has been carried out in the framework of the MAGIC-5 Collaboration, supported by the Italian *Istituto Nazionale di Fisica Nucleare* (*INFN, CSN* 5) and *ministero dell'Università e della Ricerca* (*MIUR*). We also acknowledge Drs. F. Falaschi, C. Spinelli and L. Battolla of the *U.O. Radiodiagnostica dell'Azienda Ospedaliera Universitaria Pisana* and Prof. D. Caramella and Dr. T. Tarantino of the *Divisione di Radiologia Diagnostica e Interventistica del Dipartimento di Oncologia, Trapianti e Nuove Tecnologie in Medicina dell'Università di Pisa* for providing the dataset of CT scans.

References

[1] A. Jemal, T. Murray, E. Ward, A. Samuels, R.C. Tiwari, A. Ghafoor, E.J. Feuer, M.J. Thun, Cancer statistics, 2005, CA Cancer J. Clin. 55 (2005) 10–30.
[2] A. Micheli, P. Baili, M. Quinn, E. Mugno, R. Capocaccia, P. Grosclaude, The EUROCARE Working Group, Life expectancy and cancer survival in the EUROCARE-3 cancer registry areas, Ann. Oncol. 14 (5) (2003) V28–V40.
[3] G.K. Singh, B.A. Miller, B.F. Hankey, Changing area socioeconomic patterns in US cancer mortality, 1950–1988: part II—lung and colorectal cancers, J. Natl. Cancer Inst. 94 (2002) 916–925.
[4] S. Diederich, M.G. Lentschig, T.R. Overbeck, D. Wormanns, W. Heindel, Detection of pulmonary nodules at spiral CT: comparison of maximum intensity projection sliding slabs and single image reporting, Eur. Radiol. 11 (2001) 1345–1350.
[5] S. Itoh, M. Ikeda, S. Arahata, T. Kodaira, T. Isomura, T. Kato, K. Yamakawa, K. Maruyama, T. Ishigaki, Lung cancer screening: minimum tube current required for helical CT, Radiology 215 (2000) 175–183.
[6] C.I. Henschke, D.I. McCauley, D.F. Yankelevitz, D.P. Naidich, G. McGuinness, O.S. Miettinen, D.M. Libby, M.W. Pasmantier, J. Koizumi, N.K. Altorki, J.P. Smith, Early lung cancer action project overall design and findings from baseline screening, Lancet 354 (9173) (1999) 99–105.
[7] S.J. Swensen, Screening for lung cancer with computed tomography, BMJ 326 (2003) 894–895.
[8] E.F. Patz, S.J. Swensen, J.E. Herndon, Estimate of lung cancer mortality from low-dose spiral computed tomography screening trials: implications for current mass screening recommendations, J. Clin. Oncol. 22 (2004) 2202–2206.
[9] I. Gori, F. Bagagli, M.E. Fantacci, A. Preite Martinez, A. Retico, I. De Mitri, S. Donadio, C. Fulcheri, G. Gargano, R. Magro, M. Santoro, S. Stumbo, Multi-scale analysis of lung computed tomography images, JINST 2 (2007) P09007.
[10] A. Retico, P. Delogu, M.E. Fantacci, I. Gori, A. Preite Martinez, Lung nodule detection in low-dose and thin-slice lung computed tomography, Comput. Biol. Med. 38 (4) (2008) 525–534.
[11] Q. Li, S. Sone, K. Doi, Selective enhancement filters for nodules, vessels, and airway walls in two- and three-dimensional CT scans, Med. Phys. 30 (8) (2003) 2040.
[12] 〈http://medical.nema.org〉.
[13] R. Opfer, R. Wiemker, Performance analysis for computer aided lung nodule detection on LIDC data, in: Proceedings of the SPIE 2007 Medical Imaging Conference, SPIE, vol. 6515, 2007.
[14] J.K. Leader, T.E. Warfel, C.R. Fuhrman, S.K. Golla, J.L. Weissfeld, R.S. Avila, W.D. Turner, B. Zheng, Pulmonary nodule detection with low-dose CT of the lung: agreement among radiologists, Am. J. Roentgenol. 185 (4) (2005) 973–978.
[15] M.F. McNitt-Gray, S.G. Armato III, C.R. Meyer, A.P. Reeves, G. McLennan, R.C. Pais, J. Freymann, M.S. Brown, R.M. Engelmann, P.H. Bland, G.E. Laderach, C. Piker, J. Guo, Z. Towfic, D.P. Qing, D.F. Yankelevitz, D.R. Aberle, E.J. van Beek, H. MacMahon, E.A. Kazerooni, B.Y. Croft, L.P. Clarke, The lung image database consortium (LIDC) data collection process for nodule detection and annotation, Acad. Radiol. 14 (12) (2007) 1464–1474.
[16] W.E. Lorensen, H.E. Cline, Marching cubes: a high resolution 3D surface construction algorithm, Comput. Graphics 21 (4) (1987) 163–169.
[17] B. Golosio, A. Brunetti, R. Cesareo, S.R. Amendolia, D.V. Rao, S.M. Seltzer, Images of soft materials: a 3D visualization of interior of the sample in terms of attenuation coefficient, Nucl. Instrum. Methods A 465 (2001) 577–583.
[18] D.S. Paik, C.F. Beaulieu, G.D. Rubin, B. Acar, R.B. Jeffrey, J. Yee, J. Dey, S. Napel, Surface normal overlap: a computer aided detection algorithm with application to colonic polyps and lung nodule in helical CT, IEEE Trans. Med. Imaging 23 (6) (2004) 661–675.
[19] H. Yoshida, J. Nappi, P. MacEneany, D.T. Rubin, A.H. Dachman, Computer-aided diagnosis scheme for detection of polyps in CT colonography, Radiographics 22 (2002) 963–979.
[20] National Science and Technology Research Center for Computation and Visualization of Geometric Structures The Geometry Center, University of Minnesota, 1993 〈http://www.qhull.org/〉.
[21] C.B. Barber, D.P. Dobkin, H.T. Huhdanpaa, The quickhull algorithm for convex hulls, ACM Trans. Math. Software 22 (4) (1996) 469–483.
[22] See 〈http://www.compgeom.com/meb/〉 and reference there in.
[23] M.N. Gurcan, B. Sahiner, N. Petrick, H.P. Chan, E.A. Kazerooni, P.N. Cascade, L. Hadjiiski, Lung nodule detection on thoracic computed tomography images: preliminary evaluation of a computer-aided diagnosis system, Med. Phys. 29 (11) (2002) 2552–2558.
[24] H. Arimura, S. Katsuragawa, K. Suzuki, F. Li, J. Shiraishi, S. Sone, K. Doi, Computerized scheme for automated detection of lung nodules in low-dose computed tomography images for lung cancer screening, Acad. Radiol. 11 (6) (2004) 617–629.
[25] R. Bellotti, F. De Carlo, G. Gargano, S. Tangaro, D. Cascio, C. Catanzariti, P. Cerello, S.C. Cheran, P. Delogu, I. De Mitri, C. Fulcheri, D. Grosso, A. Retico, S. Squarcia, E. Tommasi, B. Golosio, A CAD system for nodule detection in low-dose lung CTs based on region growing and a new active contour model, Med. Phys. 34 (12) (2007) 4901–4910.
[26] T. Kohonen, Self-Organization and Associative Memory, Springer, New York, 1988;
T. Kohonen, Self-Organizing Maps, Springer, New York, 1997.
[27] M. Stone, Cross-validatory choice and assessment of statistical predictions, J. R. Stat. Soc. Ser. B Methodol. 36 (1974) 111–147.
[28] C.E. Metz, ROC methodology in radiologic imaging, Invest. Radiol. 21 (9) (1986) 720–733.
[29] D.M. Green, J.A. Swets, Signal Detection Theory and Psychophysics, Wiley, New York, 1966.
[30] J.A. Hanley, B.J. McNeil, The meaning and use of the area under a receiver operating characteristic (ROC) curve, Radiology 143 (1982) 29–36.
[31] T.W. Way, L.M. Hadjiiski, B. Sahiner, H.P. Chan, P.N. Cascade, E.A. Kazerooni, N. Bogot, C. Zhou, Computer-aided diagnosis of pulmonary nodules on CT scans: segmentation and classification using 3D active contours, Med. Phys. 33 (7) (2006) 2323–2337.
[32] Y. Lee, T. Hara, H. Fujita, S. Itoh, T. Ishigaki, Automated detection of pulmonary nodules in helical CT images based on an improved template matching technique, IEEE Trans. Med. Imaging 20 (7) (2001) 595–604.
[33] S.G. Armato III, et al., The Lung Image Database Consortium Research Group, Lung image database consortium: developing a resource for the medical imaging research community, Radiology 232 (2004) 739–748.

Alessandra Retico was born in Avezzano, Italy, in 1975. She received the degree in physics in 1999 and the Ph.D. in 2002, both from the University of Rome, Italy. Since 2005, she has been with the INFN (National Institute of Nuclear Physics), Pisa, Italy, where she is a researcher in Applied Physics. Her research activity currently focuses on the development of software for data analysis and classification, with particular interest in image processing.

Maria Evelina Fantacci was born in Livorno, Italy, in 1966. She received the Degree in Physics in 1991 and the specialty degree in Medical Physics in 1994, both from the University of Pisa, Italy. Since 1997, she has been with the University of Pisa, Italy, where she is a researcher in applied physics. Her research interests focus on automated analysis of diagnostic images and development of new detectors for medical examination.

Ilaria Gori was born in Genova, Italy, in 1977. She received the degree in Mathematics from the University of Genova, in 2002 and the master degree in applied mathematics from the University of Milano Bicocca, Italy, in 2003. Since 2004, she has been with Bracco Imaging S.p.A., Milano, and Istituto Nazionale di Fisica Nucleare (INFN), Pisa, Italy, working with the Medical Physics Group of the Pisa University. Her research interests focus on computer-aided detection of pathological objects in biomedical images.

Parnian Kasae was born in Tehran, Iran, in 1977. She received the degree in biomedical engineering from the Azad University of Tehran South, Iran, in 1999 and a master degree in modeling and simulation of complex realities from International Center for Theoretical Physics (ICTP) in Trieste, Italy, in 2004. Since 2006, she has been collaborating with Istituto Nazionale di Fisica Nucleare (INFN) in Cagliari, Italy, as post-doctorate fellow working on computer aided detection systems. Her research interests focus on biomedical image processing.

Bruno Golosio was born in Nuoro, Italy, in 1971. He received the degree in physics from the University of Pisa, Italy, in 1998, and the Ph.D. from the University of Cagliari, Italy, in 2004. Since 2005, he is a researcher in physics at the University of Sassari, Italy. His research interests focus on X-ray physics, Monte Carlo simulation techniques, image reconstruction and analysis.

Alessio Piccioli was born in Verbania, Italy, in 1973. He received the degree in physics from the University of Pisa, Italy, in 1999, and the Ph.D. from the University of Siena, Italy, in 2003. He had a post-doctorate position at University of Siena, Italy, and since 2006, he has been with the University of Sassari, Italy. His research interests focus on data analysis in astroparticle and medical physics experiments.

Piergiorgio Cerello was born in Biella, Italy, in 1965. He received the degree in physics from the University of Torino, Italy, in 1989 and a Ph.D. in experimental particle physics in 1995. Since 1995, he is a researcher with the INFN (National Institute of Nuclear Physics), Italy. His research interests focus on the search for the quark gluon plasma in ion–ion collisions and on the application of software technologies developed for the high energy physics to the analysis of medical images.

Giorgio De Nunzio was born in Lecce, Italy, in 1965. He received the degree in physics from the University of Lecce in 1991, and a Ph.D. from the University of Montpellier II, France, in 1995. Since 2001, he has been with the University of Lecce, where he is a researcher in applied physics. His research interests focus on physics, informatics, and image processing, applied to medicine and cultural heritage.

Sabina Tangaro was born in 1972. She received the degree in physics from University of Pisa, Italy, and the Ph.D. in physics from University of Bari, Italy. Currently she is a researcher at INFN (National Institute of Nuclear Physics), Bari, Italy. Previously, she has been research fellow at Italian National Council of Researches and post-doctoral fellow at University of Bari. Her research interests include many topics on image processing, computer vision, pattern recognition and machine learning, with application in medicine and on medical imaging.